

Article

One–Step Synthesis of Fe–Based Metal–Organic Framework (MOF) Nanosheet Array as Efficient Cathode for Hybrid Supercapacitors

Jicheng Zhao, Liu Yang, Ruizhi Li *  and Yingke Zhou *

The State Key Laboratory of Refractories and Metallurgy, Institute of Advanced Materials and Nanotechnology, College of Materials and Metallurgy, Wuhan University of Science and Technology, Wuhan 430081, China

* Correspondence: rzli@wust.edu.cn (R.L.); zhoyk@wust.edu.cn (Y.Z.)

Abstract: With the flourishing development of the new energy automobile industry, developing novel electrode materials to balance the capacity between cathode and anode is a challenge for hybrid supercapacitors. In comparison to conventional inorganic materials, metal–organic frameworks materials offer higher porosity and greater surface area for use in supercapacitors. Herein, we proposed a facile one–pot solvothermal technique to synthesize an Fe(BPDC) nanosheet array on Ni foam, which we then applied as a binder–free cathode for a supercapacitor. The solvothermal time was adjusted to ensure a desirable morphology of the final product. Benefitting from the impressive nanosheet morphology, to a great extent, Fe(BPDC) has solved the problem of volume expansion of Fe–based electrode materials during cycling, and exhibits brilliant electrochemical performances, i.e., high specific capacitance (17.54 F/cm² at 1 mV/s) and satisfactory cycle performance (129% retention after 10,000 cycles). Furthermore, Fe(BPDC) and activated carbon (AC) have been chosen to assemble a hybrid supercapacitor (namely Fe(BPDC)//AC), delivering an energy density of 45.64 Wh/kg at the power density of 4919.6 W/kg with 87.05% capacitance retention after 10,000 cycles. These brilliant results prove that Fe(BPDC) material has great potential as the cathode of supercapacitors.

Keywords: metal–organic framework; hybrid supercapacitor; nanosheet array



check for updates

Citation: Zhao, J.; Yang, L.; Li, R.; Zhou, Y. One–Step Synthesis of Fe–Based Metal–Organic Framework (MOF) Nanosheet Array as Efficient Cathode for Hybrid Supercapacitors. *Inorganics* **2023**, *11*, 169. <https://doi.org/10.3390/inorganics11040169>

Academic Editors: Qingguo Shao and Torben R. Jensen

Received: 16 March 2023

Revised: 9 April 2023

Accepted: 13 April 2023

Published: 17 April 2023



Copyright: © 2023 by the authors. Licensee MDPI, Basel, Switzerland. This article is an open access article distributed under the terms and conditions of the Creative Commons Attribution (CC BY) license (<https://creativecommons.org/licenses/by/4.0/>).

1. Introduction

The development of energy storage technology is facing new obstacles and opportunities as a result of the global restructuring of the electric power engineering industry. With the global trend of carbon neutralization, much more new energy automobiles as well as electric buses have come into public view and become part of people’s daily life. Hence, the design and development of various new electrochemical energy storage devices in order to meet people’s needs has become one of the hot issues in the scientific research field today [1–3]. Because of the benefits of high power density, rapid charge–discharge, and long cycle life, supercapacitors are regarded as one of the most promising green energy storage devices [4]. Several types of supercapacitors are available such as electric double layer capacitors (EDLC), battery–type capacitors (BTCs), as well as pseudo–capacitors (PCs) based on various energy storage techniques [5]. EDLCs’ method of energy storage is comparable to that of conventional electrostatic capacitors. The main electrochemical reaction is a physical process of charge transfer, without complex electrochemical reaction processes [6,7]. The capacitance of PCs as well as BTCs comes from the redox reaction of surface active substances of electrode materials. Energy is stored using the quick, reversible chemical reaction between electrode materials and electrolyte ions. Hence, PCs and BTCs have higher specific capacity and energy density than EDLCs [8,9]. Hybrid supercapacitors (HSCs) interconnect the advantages of EDLCs as anode electrodes; whereas PCs, as cathode electrodes [10]. The properties of electrode materials determine supercapacitor performance. Due to their natural abundance, low cost, outstanding electrochemical

performance, and environmental friendliness, Fe-based materials have emerged as possible supercapacitor electrode materials. Zan, et al. [11] prepared a Mimosa leaf featuring reversible scatheless folding—super-foldable C-web/FeOOH-nanocone (SFCFe) conductive nanocomposites that represent cone arrays on fiber structures similar to the Mimosa leaf. The specific capacitance of SFCFe reached 152 mAh/g at 1 A/g. Zan, et al. [12] also suited a super-foldable and electrochemically functional freestanding cathode, made of C-fiber@NiS-cockscomb (SFCNi) for the first time. Its maximum area-specific capacitance reaches a high value of 1320 mF/cm² at 1 mA/cm². Tragically, the volume expansion or collapse of Fe-based electrode materials during long-term cycling led to low power density and poor stability [13]. Hence, the method of designing as well as preparing electrode materials is the key to enhancing the entire performance of supercapacitors. Currently, metal-organic frameworks materials (MOFs) with structural advantages are a potential candidate to address these issues.

MOFs are crystalline materials with a network structure that is made up of metal ions/metal clusters as well as organic ligands [14–16]. MOFs have numerous advantages such as changeable pore size, increased porosity, and increased specific surface area; the variable functional group ligands and metal ions/metal clusters lead to the diversity of structure along with the function of MOFs [17–20]. Various existing organic ligands and metal ions are suitable for MOFs synthesis, enabling MOFs materials to form 1D, 2D, as well as 3D structures to focus on the applications. Given the straightforward synthesis procedure, sizable specific surface area, flexible structure, thermal stability, and other qualities, MOFs have great development potential along with some other application prospects in the fields of catalysis, gas adsorption and separation, sensors, biomedicine, wastewater treatment, batteries, and supercapacitors [21–24]. Supercapacitors utilize MOFs to their full structural advantage because they can be used as electrodes right away. Besides, many MOFs are utilized as precursors to prepare carbon materials, metal oxides, phosphide, metal nitrides, or composites [25–33]. Furthermore, heat treatment unavoidably destroys the structure of MOFs at the expense of its advantages [34].

The synthesis strategies of MOF-based electrode materials in supercapacitors have deepened and varied more. More metals like Co, Zn, Cd, and Ni are also used as active sites in MOFs for supercapacitor electrodes. Gong, et al. [35] synthesized Zn-based and Cd-based MOFs via a hydrothermal technique along with maximum specific capacitance of 23 F/g and 22 F/g. It demonstrated that the performance of supercapacitors was enhanced by the considerable porosity of MOFs. Yang, et al. [36] further doped Zn(II) into Ni-based MOF; the specific capacitance reached 1620 F/g at 0.25 A/g, which demonstrated that the fabrication of MOFs could still benefit from the synergistic action of bimetals. MOFs (UiO-66 family) of Zr (IV) have greatly expanded the application field of MOFs because of their excellent thermal stability along with the stability of solvents (water, ethanol, and N, N-dimethylformamide) [37]. This work proved that metal ions with strong ligands and high valence can indeed increase MOF stability. Hangarter, et al. [38] prepared and compared 23 various nanocrystalline MOFs (nMOFs) and added these nMOFs to the electrodes of supercapacitor devices. Between them, nMOF-867 with great chemical as well as thermal stability represented the highest electrochemical activity (5085 mF/cm²). Wang, et al. [39] compounded Co-MOF with reduced diluted graphite oxide, and mild alkali was used to activate the resultant composite such as LiOH, showing good specific capacitance. Nevertheless, the material exhibited self-activation characteristics, and as the number of cycles increased, the specific capacitance increased until it reached 1200. This was because composite materials could form Li[CoOH] (BDC) containing phthalate radicals (BDC) under alkaline conditions, and CoOH was easily formed after power-on, that significantly increased the capacitance of the electrode materials. Nicolò, et al. [40] tried to mix Fe-based MOF (MIL-100, MIL-88, and MIL-53) with carbon nanotubes as well as carbon black as electrode materials for supercapacitors, and analyzed the valence state of Fe. It was discovered that the Fe center in MIL-100 was in the state of Fe³⁺; which, would

partly be transformed into Fe^{2+} or iron trimer in the process of energy storage. As a result, a rationale for using Fe-based MOFs for capacitor energy storage was established.

Although the pristine MOF along with its derivatives have flourished in the application field of supercapacitor electrode materials, their chances for development are nevertheless inevitably limited by their weak conductivity [41]. Currently, most MOFs for energy storage electrodes are assembled using powder materials utilizing polymer adhesives and additives, which causes aggregation of active materials [42]. However, the materials used in the array are devoid of binder, which can increase surface area, speed up ion diffusion, and improve electronic conductivity without the use of additional conductive agents or additives. Among many MOFs, Fe-based MOFs have many applications in various fields like catalysis, gas adsorption along with separation, antibiotic removal, etc. [43–45]. However, there is little research in the direction of supercapacitors. Fe compounds exhibit fantastic electrochemical activity and many valence states. Fe has a high rate of redox active sites, which have a theoretically high specific capacity, showing that Fe-based MOFs are an excellent candidate for energy storage materials [46,47]. Somehow, the application of Fe materials in supercapacitors has been hampered by its inadequate conductivity, volume expansion, and unsatisfactory cycle performance. Only by solving the following issues, will we be able to enhance the development potential of Fe materials. Furthermore, the preparation technique of MOFs is relatively cumbersome in past studies, which limits its practical application. Consequently, streamlining the preparation process and increasing output efficiency are both very important.

On the basis of above reasons, 4,4'-biphenyldicarboxylic acid was selected in order to synthesize Fe(BPDC) nanosheet arrays on Ni foam by solvothermal strategy. It is important to note that by adjusting various solvothermal time lengths, we altered the morphology of the samples (3 h, 6 h, 12 h, 18 h), named as Fe(BPDC)-1, Fe(BPDC)-2, Fe(BPDC)-3, Fe(BPDC)-4. After various characterization as well as electrochemical tests, Fe(BPDC)-3 was determined as the best sample. The Fe(BPDC)-3 electrode displayed superior cycling performance with 129% retention after 10,000 cycles along with extremely high specific capacitance of 17.54 F/cm^2 at 1 mV/s . Additionally, the Fe(BPDC)//AC hybrid supercapacitor was developed, which exhibited 1.9 V high-voltage and also presented an energy density of 45.64 Wh/kg at the power density of 4919.6 W/kg along with long cycle life (86.41% after 10,000 cycles). The huge potential for employing MOF cathode materials in high-performance hybrid supercapacitors is demonstrated by these favorable results.

2. Results and Discussion

To explore the growth mechanism of Fe(BPDC) nanosheet array, a series of experiments concerning solvothermal reaction time were conducted. Figure 1 shows the synthesis process and coordination mode. After $125 \text{ }^\circ\text{C}$ solvothermal, Fe(BPDC) in-situ grows vertically arranged, uniformly dispersed interconnected nanosheet arrays on the surface of Ni foam. Each Fe atom is six-coordinated, with four H_2O molecules and two oxygen atoms in biphthalic acid, respectively.

It is noteworthy that the nanosheets change according to the solvothermal time. The morphology of Fe(BPDC)-1 and Fe(BPDC)-2 are shown in Figure S1a–d; when the solvothermal time reached 3 h, the Ni foam surface has the trend of sheet morphology formation, slight aggregation, and obviously shorter sheet length. When the solvothermal time was up to 6 h, the surface of Ni foam begins to form a sheet shape by vertical growth but still slightly shorter length, which is more uniform than Fe(BPDC)-1. As shown in Figure 2a,b, when the solvothermal time reached 12 h, the surface of Ni foam grows a continuous and uniform sheet shape. Fe(BPDC)-3 shows the best dispersion, size uniformity, and integrity. The sheets length is about $800 \text{ }\mu\text{m}$ with the thickness of about 38.5 nm . The 3D structure of the Ni foam carrier itself and the lamellar morphology of Fe(BPDC)-3 form a hierarchical structure, which can greatly improve the specific surface area of active materials and promote the penetration of electrolytes. When the solvothermal time reached 18 h, as shown in Figure S1e,f, the nanosheets morphology of Fe(BPDC)-4 is further ex-

tended and tangled together. In order to further view the structure and morphology of Fe(BPDC)–3, TEM was used to observe the sample. As shown in Figure 2c,d, the obvious connected nanosheets can be seen, and metal ion clusters are uniformly dispersed in the sheet morphology and connected by coordination bonds. The high-resolution TEM image (HRTEM) in Figure 2e shows that the lattice distance about 1.936 Å denoted the (010) planes of MIL–88D(Fe) [48]. The energy-dispersive X-ray spectroscopy (EDX) and mappings (Figure 2f) confirm the existence of Fe, C, O, Ni. We can find that there is a small amount of Ni involved in the reaction. This is because Fe^{3+} corrodes the Ni foam and causes Ni^{2+} to separate out in the reaction, corresponding to selected-area electron diffraction (SAED), inset Figure 2e. For comparison, comparative experiments were conducted under the same conditions, but $\text{Fe}(\text{NO}_3)_3 \cdot 9\text{H}_2\text{O}$ were not introduced; respectively, shown as Figure S1g,h, we can find that the morphology is the same as the blank Ni foam, which indicates that the formation of sheet morphology is due to the interaction and coordination between $\text{Fe}(\text{NO}_3)_3 \cdot 9\text{H}_2\text{O}$ and BPDC. To investigate the surface area and pore size, BET was characterized for the Fe(BPDC)–3 in Figure S2. The BET isotherm characteristic curve suggests an IV type graph for the Fe(BPDC)–3. The pores are mainly distributed at approximately 4 nm. This indicates the presence of mesopores in our material which can facilitate better electrochemical storage.

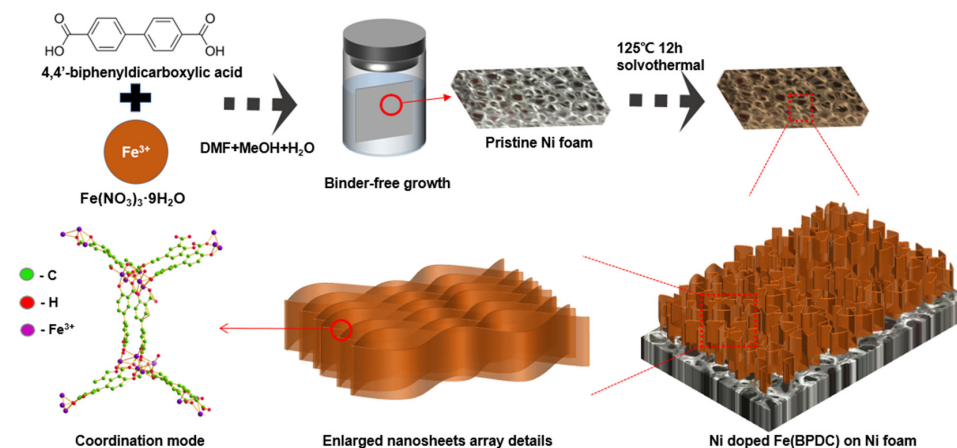


Figure 1. Working procedure and coordination environment of Fe^{3+} in Fe(BPDC).

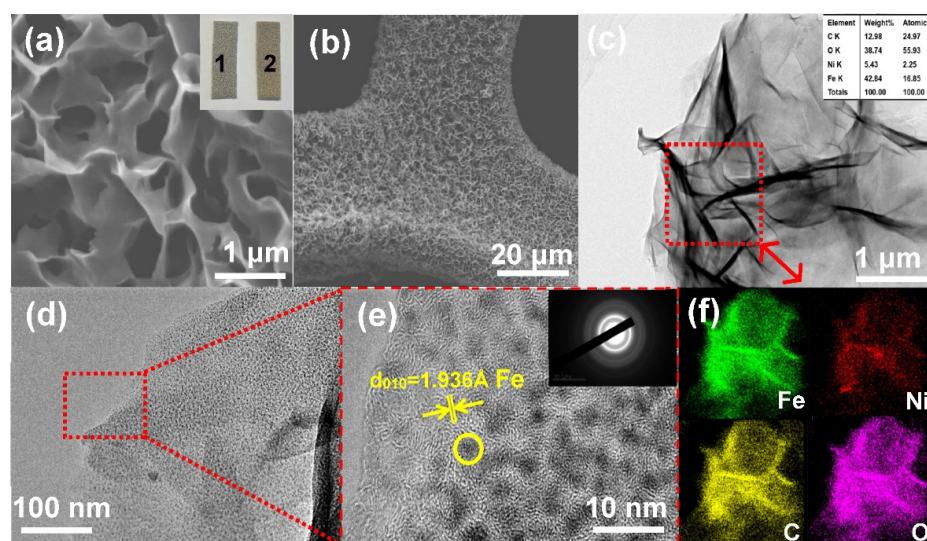
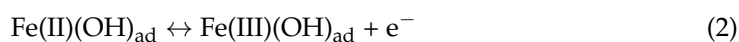
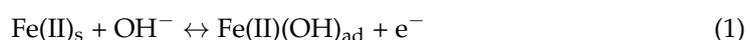


Figure 2. (a,b) SEM images of Fe(BPDC)–3. (Inset: optical image of 1 blank Ni foam, 2 Fe(BPDC)–3). (c,d) TEM and (e) HRTEM images of Fe(BPDC)–3, respectively. (Inset: EDX element content). (f) Elemental mapping results of Ni, Fe, C, and O, respectively. (Inset: FFT patterns of the selected areas).

Figure 3a shows the X-ray diffraction (XRD) patterns of Fe(BPDC) compared with the simulated XRD patterns of Fe(BPDC) produced by the crystal X-ray data using the Diamond 4 software. The XRD curves of Fe(BPDC) closely resemble the simulated diffraction pattern and shows pronounced Ni foam characteristic peaks, which indicates that we have successfully synthesized MOFs on Ni foam. The newly synthesized Fe(BPDC) crystal is isomorphic to the reported [Co(bpdc)(H₂O)₂]₂H₂O [49], and the X-ray diffraction peak of the Fe(BPDC) is consistent with the reported simulated peak of MIL-88D(Fe)(CCDC: 285811) [48]. In order to further prove the existence of coordination bond, we carried out FT-IR to test the sample. FT-IR spectra of Fe(BPDC) are provided in Figure 3b. It can be clearly seen that the absorption peak at 3434 cm⁻¹ corresponds to the O–H tensile vibration of the carboxyl group of the coordination water molecule. The peak observed at 1685 cm⁻¹ can be attributed to the C=O tensile vibration of the carboxyl group. The strong absorption band between 1607 and 1296 cm⁻¹ belongs to the skeleton vibration of aromatic ring. In addition, the peaks at 759 cm⁻¹ and 555 cm⁻¹ are related to the C–H bond vibration of benzene ring and the formation of metal–O bond between the carboxyl group of BPDC and Fe³⁺ ions. This result further demonstrates the formation of MOFs. The elemental composition and valence state of the Fe(BPDC) nanosheet array was further demonstrated by XPS. The inset in Figure 3c is the full survey spectrum of Fe(BPDC)–3. It confirms the presence of C, O, Ni, and Fe elements. The existence of Ni is because Fe³⁺ corrodes the Ni foam and causes Ni²⁺ to separate out in the solvothermal reaction. This indicates that there is a small amount of Ni is involved in the reaction and is consistent with TEM results. The peak positions of Fe 2p elements are corrected by C 1 s spectra and the standard is based on the 284.8 eV binding energy of C 1 s. The C 1 s spectrum of Fe(BPDC) is shown in Figure 3c. The peaks at 286.0 and 288.4 eV are assigned to the aryl carbon from the benzene ring and the carboxylate carbon in O=C–OH and the peaks at 292.2 eV due to the π–π transition. In the O 1 s region (Figure 3d), two O 1 s peaks at 531.9 and 533.5 eV are relevant to C=O and C–O units of the carboxylic group of the BPDC. Meanwhile, the Fe–O peak appearing at 530.1 eV also confirm the coordination behavior. In the Fe 2p region (Figure 3e), the two peaks at 711.4 and 725.0 eV can be assigned to Fe 2p_{3/2} and Fe 2p_{1/2}, respectively. The BEs of 733.7 and 719.5 eV with two shakeup satellites (identified as “Sat.”) also correspond to the Fe³⁺. The peaks of Fe 2p_{3/2} can be deconvoluted into two peaks, which are caused by the splitting of the spin–orbit related to the bending energy of the satellite peak [50]. The Ni 2p XPS spectrum (Figure 3f) shows double peaks at 856.4 eV and 874.2 eV, corresponding to Ni 2p_{3/2} and Ni 2p_{1/2}, and the peaks at 881.6 eV and 862.3 eV correspond to two satellite peaks. The result implies the presence of Fe, C, O, and Ni without other impurities in Fe(BPDC).

2.1. Electrochemical Performances

The electrochemical properties of Fe(BPDC) with different solvothermal times were tested in a three-electrode system using 3 M KOH as the electrolyte. Figure 4 shows the effect of different solvothermal reaction times on the electrochemical performance of Fe(BPDC). CV curves in Figures 4a and S3 that the voltage window of Fe(BPDC) is 0–0.55 V. Two redox peaks were clearly observed on all CV curves, which correspond to the valence state transition of Fe³⁺/Fe²⁺ during charging and discharging, indicating the typical faradic characteristics. With the increase in scan rate, the integral area of the CV curve of Fe(BPDC) also gradually increases, and the obvious redox peak can still be maintained at a high scan rate, indicating that the electrode has a faster redox reaction. The possible redox reaction of Fe(BPDC) electrode can be summarized as:



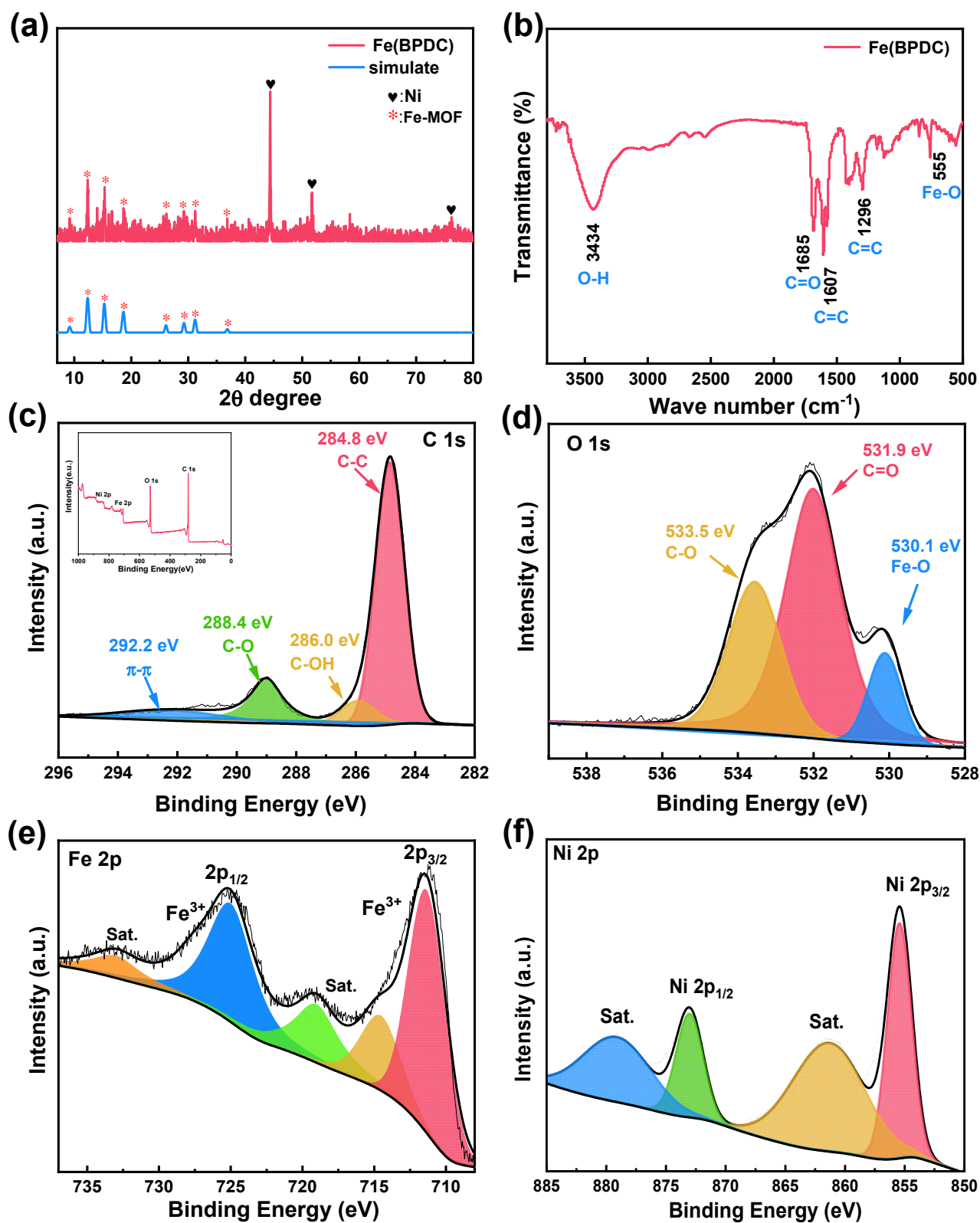


Figure 3. Characterization. (a) XRD patterns of Fe(BPDC)-3. (b) FT-IR spectra of Fe(BPDC)-3. High-resolution XPS spectra of (c) C 1s, (d) O 1s, (e) Fe 2p, (f) Ni 2p of Fe(BPDC)-3, respectively. (Inset in (c) is the XPS total spectrum).

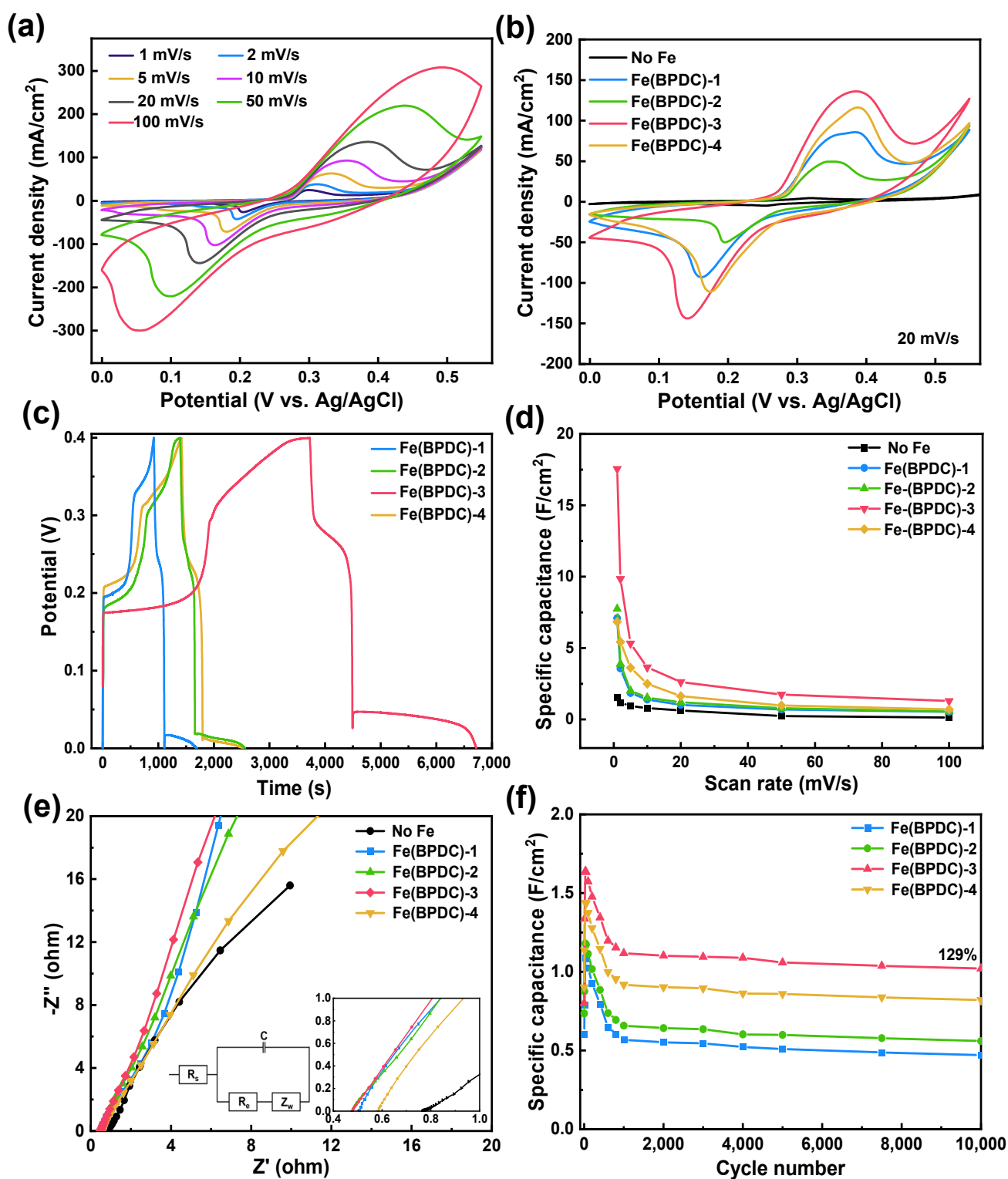


Figure 4. (a) CV curves of Fe(BPDC)-3 at a scan rate of 1 mV/s to 100 mV/s. (b) CV curves at a scan rate of 20 mV/s. (c) GCD curves at the current density of 2 mA/cm². (d) The specific capacitance of Fe(BPDC)-X at different current densities. (e) EIS curves of Fe(BPDC)-X. (f) Cycling stability of the Fe(BPDC)-X electrode.

Figure 4b shows the CV curves' comparison of Fe(BPDC) with different solvothermal times at a scan rate of 20 mV/s. The CV curves of the as-synthesized samples show similar redox peaks, and it is obvious that Fe(BPDC)-3 samples have a larger CV curve

integral area than the other three samples, proving significantly higher electrochemical activity and capacitance. This is due to the homogeneous morphology and larger specific surface area of Fe(BPDC)-3, which are consistent with the results of SEM. Figure 4c shows the charge–discharge (GCD) curves of Fe(BPDC) with different solvothermal times at the current density of 2 mA/cm². It can be seen that Fe(BPDC)-3 has a longer discharge time, proving that it has a higher specific capacity. The charging time was almost equal to the discharging time, indicating that Fe(BPDC)-3 has coulombic efficiency and highly reversible redox reactions in GCD. There is an obvious platform in the discharge curve, indicating a pseudocapacitive feature of the Fe(BPDC) electrode material, which conforms to the results of CV curve. The redox reaction and electrochemical adsorption/desorption process at the electrode/electrolyte interface are frequently responsible for the emergence of the charge–discharge platform. The specific capacitance was calculated for electrodes with different solvothermal reaction times, as shown in Figure 4d. The Fe(BPDC)-3 nanosheet array electrode always exhibits the highest specific capacitance. The faster the scan rate, the lower the specific capacity of the electrode is because the migration of ions cannot respond to the speed of the redox reaction. Specifically, At 1 mV/s, it delivers 17.54 F/cm² (9.65 C/cm²)—much higher than other sample (Fe(BPDC)-1: 7.10 F/cm²; Fe(BPDC)-2: 7.74 F/cm²; Fe(BPDC)-4: 6.83 F/cm²). To further study the ion and electron transport kinetics of the Fe(BPDC) electrodes, electrochemical impedance spectroscopy (EIS) measurements with equivalent circuits are shown in Figure 4e. R_e and R_{ct} of Fe(BPDC)-X are much better than the Ni foam samples without the Fe source. This is due to the hierarchical structure formed by the lamellar morphology of Ni foam with a 3D structure and Fe(BPDC), which is more conducive to charge transfer and transmission. While Fe(BPDC)-3 has a more uniform morphology and larger specific surface area, its EIS curve shows the smallest R_{ct} (0.019 Ω) and a relatively small R_e (0.477 Ω), proving that it has the best charge transfer performance and moderate ion diffusion. In addition to the capacity, cycling performance is also a key factor in determining the practical application of the materials. The cycling performance of Fe(BPDC)-X was tested at 50 mV/s for 10,000 cycles, as shown in Figure 4f. The increase in specific capacitance at the beginning could be attributed to the activation of Fe(BPDC)-X. The contact between the electrolyte and the active material gradually becomes complete, and more redox reactions occur. The specific capacitance of the electrode material will reach its maximum and gradually decrease. In all as-prepared samples, Fe(BPDC)-3 exhibit excellent cycling performance of 129% retention after 10,000 cycles. This is due to the close combination of Fe ions and ligands. Commonly, an excessively thin nanosheets layer has a weak effect on maintaining structural stability; while, an excessively thick nanosheets layer will hinder the reaction of inside electrode material, resulting in lower specific capacitance.

The specific capacity and cycle performance of the Fe(BPDC)-3 material in this work are found to be significantly better than most published cathode materials when compared to other Fe-containing electrode materials and MOFs electrode materials (Table S1). For instance, Fe(TATB)(Tpa)(H₂O) (409.2 C/g) [50], Fe-MOF/Ni(OH)₂ (676.8 C/g) [51], NFCS-NS (1156 C/g) [52], Fe-Co-S/NF (2695 F/g) [53], u-hl-MOF/NRSs (13.14 F/cm²) [54], and Ni-MOF@NCS/NF (14.5 F/cm²) [55]. The excellent electrochemical performance of the Fe(BPDC) electrode can be explained by the following aspects. (1) Due to the Ni's similar ionic radius to that of Fe, a little portion of Ni has replaced the Fe's central location. Moreover, the crystallinity of the Fe-based MOFs is enhanced after Ni ion doping. Efficiently buffering the volume strain of the electrode material during frequent charging and discharging can increase the stability of the electrode material. (2) The synergistic effect of bimetals. The doping of Ni metal nodes can effectively promote the electronic coupling between metal nodes to improve the electronic conductivity between the electrode and the electrolyte surface. The doping of Ni also provides more active sites for the oxidation–reduction reaction of MOFs materials; thus, bringing ultra-high specific capacitance. (3) Fe(BPDC) is grown on the three-dimensional conductive substrate Ni foam without any additives and binders, which enables the direct transfer of electrons and ions

between the electrode material and the substrate; effectively, enhancing the transmission of electrons and ions and shortening the diffusion distance of electronic ions. (4) The active material does not easily fall off or collapse during the long cycle test due to the strong adhesion of the nanostructured material to the Ni foam, which guarantees the mechanical stability and long cycle stability of the electrode material. Notably, during the electrochemical reaction, the uncoordinated carboxylic acid O group and the coordinated H₂O molecule can interact molecularly to adsorb/desorb the hydroxide ion in the electrolyte; thus, supplying a channel for ion transport. The high specific capacity and excellent cycling performance all show that Fe(BPDC) material has strong competitiveness in the field of supercapacitor cathodes.

2.2. Fabrication of Hybrid Supercapacitor

An all-solid-state hybrid supercapacitor was assembled using Fe(BPDC)-3 as the cathode and activated carbon (AC) as the anode to further demonstrate the practical applicability of the generated electrode materials. To build the device, PVA/KOH gel was chosen as the electrolyte and polyacrylate sodium (PAAS) as the water-retaining agent, with PAAS efficiently preventing water loss during testing. The CV curves of Fe(BPDC)//AC are shown in Figure 5a. The voltage range of Fe(BPDC)//AC is 0–1.9 V and the curve shape is similar to a rectangle without obvious redox peaks, displaying double-layer capacitance behavior, which indicates that the hybrid supercapacitor is well-matched. Specific capacitance of 26.45 F/cm² at 1 mV/s clearly shows the potential for future hybrid devices. Besides, the GCD test of the device was also carried out at a current density of 10–60 mA/cm² (Figure 5b). The GCD curve shows a slightly biased triangle-like shape, indicating that the device has good electrochemical reversibility and ideal capacitive behavior. Over such a wide voltage range, cycle performance should be viewed as important as capacitance. Figure 5c shows the EIS diagram of Fe(BPDC)//AC. The EIS curve shows a small R_{ct} (0.019 Ω), relatively small R_e (0.477 Ω), and the diffusion resistance R_w is steep, indicating that Fe(BPDC)//AC has excellent charge transfer performance and moderate ion diffusion; which, is consistent with the electrochemical test results such as CV and CD. Energy density and power density are two significant characteristics to consider when evaluating the energy storage capability of supercapacitors. Hence, the power density and energy density of the Fe(BPDC)//AC are calculated and plotted as Ragone plots, as shown in Figure 5d. The power density is 4919.6 W/kg at an energy density of 45.64 Wh/kg while the energy density is 99.86 Wh/kg at a power density of 836.00 W/kg. Compared with the energy density of other previously reported HSCs with Fe-containing electrode materials (Table 1), our results are superior to those of Fe-ASC (12,000 W/kg at 22 Wh/kg) [50], MOF@Ni(OH)₂-20/NF//AC/NF (800 W/kg at 67.1 Wh/kg) [51] NiCoP//AC (2250 W/kg at 36.87 Wh/kg) [52], Fe-Co-S//rGO (770 W/kg at 43.6 Wh/kg) [53], Ni-MOF@NCS//AC (363.7 W/kg at 58.8 Wh/kg) [55], AC//Co-MOF@Co (145.1 W/kg at 43.4 Wh/kg) [56], AC//MOF/PANI (600 W/kg at 23.11 Wh/kg) [57], NFCS-NS//AC (807.04 W/kg at 57.3 Wh/kg) [58], and Ni-MOF@ppy//AC (1500.6 W/kg at 40.1 Wh/kg) [59]. The cycle stability of Fe(BPDC)//AC is tested at 50 mV/s as shown in Figure 5e. After 10,000 cycles, the capacity retention rate of Fe(BPDC)//AC is 86.41%, which shows excellent cycle stability. In addition, to verify the practical application of Fe(BPDC)//AC, two assembled electrochemical devices in series can light up a small bulb with a rated voltage of 2 V for 30 min (inset Figure 5e). Good temperature adaptability can extend the service life of hybrid supercapacitors in various climates; which, is of great significance to the large-scale popularization of supercapacitors. Here, we test the capacitance of Fe(BPDC)//AC at different temperatures, starting from -10 °C, rising to 100 °C, and then control the temperature back to -10 °C, as shown in Figure 5f. In the process of temperature change from low to high and then returning, the capacity curve basically remains flat and slightly decreases in the process of temperature returning, which confirms that Fe(BPDC)//AC has excellent temperature adaptability and robust application performance.

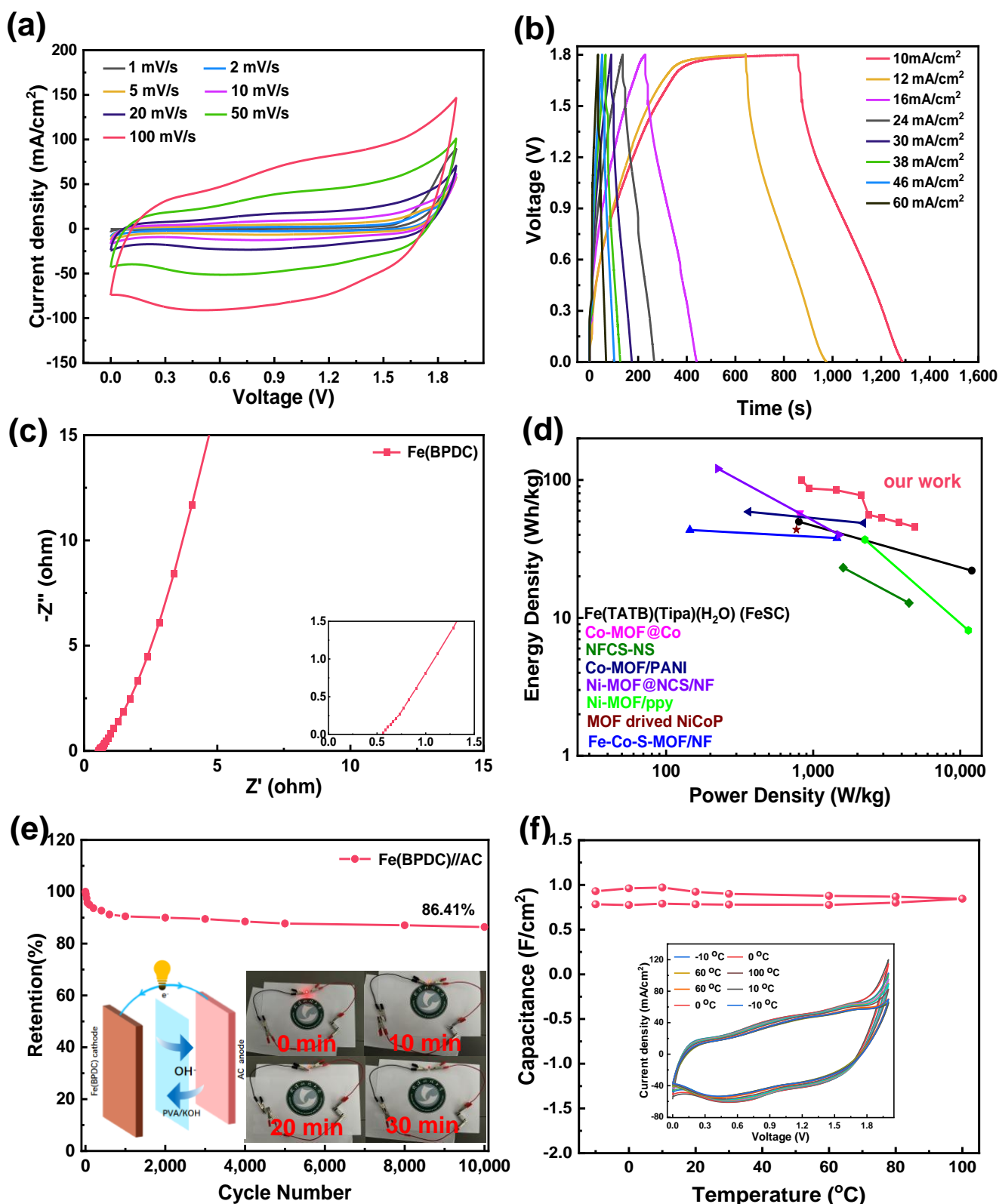


Figure 5. (a) CV curves of the Fe(BPDC)//AC at the scan rate of 1 to 100 mV/s. (b) GCD curves at different current densities of Fe(BPDC)//AC. (c) EIS spectra of Fe(BPDC)//AC. (d) Ragone plot comparison of our Fe(BPDC)//AC with some reports in the literature. (e) Cycling stability of Fe(BPDC)//AC. (Inset: image of a bulb (2 V) lit up for different periods of times, respectively. (f) Capacitance at different temperatures. (Inset: CV curves at different temperatures).

Table 1. Comparison of Fe(BPDC)//AC with recently published MOFs devices.

HSC	Voltage Range (V)	Energy Density (Wh/kg)	Power Density (W/kg)	Number of Cycles	Capacitance Retention (%)	Year [Reference]
Fe-ASC	0–1.7	22	12,000	6000	90.6	2021 [50]
Fe-MOF@Ni(OH) ₂ -20/NF//AC/NF	0–1.6	67.1	800	4000	100	2021 [51]
NiCoP//AC	0–1.6	58.8	781.3	10,000	96.2	2021 [52]
Fe-Co-S/NF//rGO	0–1.6	43.6	770	5000	89.6	2019 [53]
Ni-MOF@NCS/NF//AC	0–1.7	58.8	363.7	10,000	96.2	2021 [55]
AC//Co-MOF@Co	0–1.7	43.4	145.1	10,000	87.5	2021 [56]
AC//MOF/PANI	0–1.6	23.11	600	3000	146	2020 [57]
NFCS-NS//AC	0–1.6	57.3	807.04	10,000	90.8	2020 [58]
Ni-MOF-ppy//AC	0–1.5	40.1	1500.6	10,000	80	2020 [59]
Fe(BPDC)//AC	0–1.9	45.64 99.85	4919.55 835.1	10,000	86.41	This work

3. Materials and Methods

3.1. Synthesis of Fe(BPDC) Nanosheet Arrays Cathode

Ni foam was cleaned ($3.7 \times 5 \text{ cm}^2$) with 2 M hydrochloric acid (HCl), ethanol, and deionized water for 15 min, respectively, then put it into a 60 °C oven to dry. Fe(BPDC) nanosheet arrays on Ni foam were synthesized via solvothermal strategy. Typically, 0.484 g (2 mmol) of 4,4'-biphenyldicarboxylic acid (BPDC) was dispersed in 60 mL N,N-dimethylformamide (DMF) solution under stirring. Subsequently, 0.808 g (2 mmol) of $\text{Fe}(\text{NO}_3)_3 \cdot 9\text{H}_2\text{O}$ was dissolved in the 4,4'-biphenyldicarboxylic solution. Then, 5 mL ethanol and 5 mL deionized water were added drop by drop and put the mixed solution into the ultrasonic machine for 15 min to fully dissolve. The above mixture solution and the treated Ni foam were transferred to 100 mL autoclave. Finally, the autoclave was kept at 125 °C for 3 h, 6 h, 12 h, 18 h, respectively, and then naturally cooled to room temperature. Finally, the achieved Fe(BPDC) samples were washed with ethanol and deionized water and dried at 60 °C overnight. The mass loading is 1.03 mg, which is determined by the weight difference between Fe(BPDC) and blank Ni foam. For comparison, comparative experiments were conducted under the same conditions, but $\text{Fe}(\text{NO}_3)_3 \cdot 9\text{H}_2\text{O}$ was not introduced, respectively.

3.2. Fabrication of Fe(BPDC)//AC Hybrid Supercapacitors

The preparation method of AC electrode: mixing activated carbon (AC), polyvinylidene fluoride (PVDF), and acetylene black at a ratio of 8:1:1; grinding for 20 min; then adding NMP, stirring for 30 min; the slurry was coated on the cleaned blank Ni foam and dried in the oven at 60 °C overnight. The PVA/KOH solid electrolyte was prepared as follows: 6 g PVA (1799 type) was dissolved in 50 mL deionized water and stirred vigorously for 1 h at 90 °C until a transparent and uniform sol was formed; 6 g of potassium hydroxide (KOH) was dissolved in 5 mL of deionized water and transferred to the PVA sol drop by drop, and stirred at 90 °C for 15 min; finally, 2 mL of sodium polyacrylate (PAAS) was added to the above solution and stirred at 85 °C for 15 min. Fe(BPDC) cathode and AC anode were coated with appropriate PVA-KOH gel electrolyte, then assembled face-to-face and for solidification. The total mass loading of Fe(BPDC)//AC is 9.03 mg/cm^3 .

3.3. Morphology and Structure Characterization

Morphology and phase characteristics of the as-synthesized samples were characterized by scanning electron microscope (SEM, PHILIPS XL30 TMP, Davis, CA, USA), transmission electron microscope (TEM, JEOL JEM-2000 UHR SETM/EDS, Tokyo, Japan) (include energy dispersive X-ray spectroscopy (EDX), selected area electron diffraction

(SAED) elemental mapping), X-ray powder diffraction (XRD), X-ray photoelectron spectroscopy (XPS, ThermoScientific Escalab 250Xi, Waltham, MA, USA), and Fourier infrared spectrometer (ThermoScientific Nicolet iS50, Waltham, MA, USA). The mass loading was calculated by a semi-micro balance (ESJ200-4B) with a readability of 0.001 mg.

3.4. Electrochemical Measurements

All electrochemical tests in this experiment (three electrodes/two electrodes) were performed on the BioLogic VMP3 electrochemical workstation. The Fe(BPDC) was directly used as the working electrode with the Pt plate (1 cm × 1 cm) as the counter electrode and the Ag/AgCl electrode as the reference electrode in 3 M KOH solution. Scan rates of the cyclic voltammetry (CV) were 1~100 mV/s. Electrochemical impedance spectroscopy (EIS) was tested between 0.01 Hz and 100 kHz.

The specific capacity of Fe(BPDC) was calculated according to CV curve using (3):

$$C = \frac{\int I(V)dV}{2vAV} \quad (3)$$

where $I(V)$ is the current at V , dV is differential potential, v is the scan rate, V is the potential window, A is the electrode's surface area (or mass of the active materials).

The energy and power densities (E and P) of the solid-state device were calculated using (4) and (5):

$$E = \frac{I \int V(t)dt}{T} \quad (4)$$

$$P = E / \Delta t \quad (5)$$

where I is the discharging current, $V(t)$ is discharging voltage at t , dt is time differential, T is the volume of the device, and Δt is the total discharging time.

4. Conclusions

In summary, Fe(BPDC) nanosheet array was successfully synthesized on Ni foam via the one-pot solvothermal method. By regulating the solvothermal time, an optimized Fe(BPDC)-3 electrode was fabricated with an ultrahigh specific capacitance up to 17.54 F/cm² at 1 mV/s and an excellent cycling stability with 129% retention after 10,000 cycles. Furthermore, a hybrid supercapacitor was assembled with Fe(BPDC)-3 and AC as the cathode and anode materials, respectively. The as-fabricated supercapacitor has a high specific capacity of 26.45 F/cm², delivering the highest energy density of 45.64 Wh/kg and the capacity retention remains 86.41% after 10,000 cycles. These impressive results grant the potential of the Fe(BPDC) electrode as a promising cathode for energy storage, and its preeminent environmental adaptability also provides a new idea for the large-scale popularization of new energy vehicles in the future.

Supplementary Materials: The following supporting information can be downloaded at: <https://www.mdpi.com/article/10.3390/inorganics11040169/s1>, Figure S1: SEM images of (a,b) Fe(BPDC)-1, (c,d) Fe(BPDC)-2, (e,f) Fe(BPDC)-3, (g,h) sample without iron source; Figure S2: BET analysis of the Fe(BPDC)-3; Figure S3: CV curves of (a) Fe(BPDC)-1, (b) Fe(BPDC)-2, (c) Fe(BPDC)-3 electrode; Table S1: Comparison of Fe(BPDC)-3 with published MOFs cathode; Figure S4: GCD curves at different current densities of Fe(BPDC)-3; Figure S5: (a) Comparison of CV curves at 20mV/s of Fe(BPDC)-3 and AC. (b) Capacitance of Fe(BPDC)//AC.

Author Contributions: Writing—original draft preparation, J.Z.; formal analysis and data curation, J.Z. and L.Y.; writing—review and editing, R.L.; supervision and funding acquisition, R.L. and Y.Z. All authors have read and agreed to the published version of the manuscript.

Funding: This research was funded by the National Natural Science Foundation of China (no. 51802233).

Data Availability Statement: Not applicable.

Conflicts of Interest: The authors declare no conflict of interest.

References

1. Lu, X.F.; Li, G.; Tong, Y. A review of negative electrode materials for electrochemical supercapacitors. *Sci. China Technol. Sci.* **2015**, *58*, 1799–1808. [[CrossRef](#)]
2. Mustafa, E.S.; Frede, B.; Ariya, S. A Comprehensive Review on Supercapacitor Applications and Developments. *Energies* **2022**, *15*, 674.
3. Wang, H.-Y.; Li, B.; Teng, J.-X.; Zhu, H.-L.; Qi, Y.-X.; Yin, L.-W.; Li, H.; Lun, N.; Bai, Y.-J. N-doped carbon-coated TiN exhibiting excellent electrochemical performance for supercapacitors. *Electrochim. Acta* **2017**, *257*, 56–63. [[CrossRef](#)]
4. Li, B.; Pang, H.; Xue, H. Fe-based phosphate nanostructures for supercapacitors. *Chin. Chem. Lett.* **2020**, *32*, 885–889. [[CrossRef](#)]
5. Wu, Y.; Ran, F. Vanadium nitride quantum dot/nitrogen-doped microporous carbon nanofibers electrode for high-performance supercapacitors. *J. Power Sources* **2017**, *344*, 1–10. [[CrossRef](#)]
6. Nithya, V. A review on holey graphene electrode for supercapacitor. *J. Energy Storage* **2021**, *44*, 103380. [[CrossRef](#)]
7. Kumar, R.D.; Nagarani, S.; Sethuraman, V.; Andra, S.; Dhinakaran, V. Investigations of conducting polymers, carbon materials, oxide and sulfide materials for supercapacitor applications: A review. *Chem. Pap.* **2022**, *76*, 3371–3385. [[CrossRef](#)]
8. Mani, M.P.; Ponnarasi, K.; Rajendran, A.; Venkatachalam, V.; Thamizharasan, K.; Jothibas, M. Electrochemical Behavior of an Advanced FeCo₂O₄ Electrode for Supercapacitor Applications. *J. Electron. Mater.* **2020**, *49*, 5964–5969. [[CrossRef](#)]
9. Ravikant, A.; Meenakshi, S.; Siddharth, S.; Ashwani, K.; Gaurav, M.; Rabah, B.; Ramesh, C. Metal nitrides as efficient electrode material for supercapacitors: A review. *J. Energy Storage* **2022**, *56*, 105912.
10. Chatterjee, D.P.; Arun, K.N. A review on the recent advances in hybrid supercapacitors. *J. Mater. Chem. A* **2021**, *9*, 15880.
11. Zan, G.T.; Wu, T.; Zhang, Z.L.; Li, J.; Zhou, J.C.; Zhu, F.; Chen, H.X.; Wen, M.; Yang, X.C.; Peng, X.J.; et al. Bi-inspired Nanocomposites with Self-Adaptive Stress Dispersion for Super-Foldable Electrodes. *Adv. Sci.* **2021**, *9*, 2103714. [[CrossRef](#)] [[PubMed](#)]
12. Zan, G.; Wu, T.; Dong, W.; Zhou, J.; Tu, T.; Xu, R.; Chen, Y.; Wang, Y.; Wu, Q. Two-Level Biomimetic Designs Enable Intelligent Stress Dispersion for Super-Foldable C/NiS Nanofiber Free-Standing Electrode. *Adv. Fiber Mater.* **2022**, *4*, 1177–1190. [[CrossRef](#)]
13. Rasmita, B.; Nafiseh, M.; Kam, T.L.; Mamata, M. Effect of synthesis parameters on tuning of phase and shape of hierarchical iron oxides and selective application as supercapacitor. *Ionics* **2019**, *25*, 1793–1803.
14. O'keeffe, M.; Yaghi, O.M. Deconstructing the Crystal Structures of Metal-Organic Frameworks and Related Materials into Their Underlying Nets. *Chem. Rev.* **2011**, *112*, 675–702. [[CrossRef](#)]
15. Jiao, Y.; Pei, J.; Yan, C.S.; Chen, D.H.; Hu, Y.Y.; Chen, G. Layered nickel metal-organic framework for high performance alkaline battery-supercapacitor hybrid devices. *J. Mater. Chem. A* **2019**, *4*, 13344–13351. [[CrossRef](#)]
16. Salunkhe, R.R.; Kaneti, Y.V.; Yamauchi, Y. Metal-Organic Framework-Derived Nanoporous Metal Oxides toward Supercapacitor Applications: Progress and Prospects. *ACS Nano* **2017**, *11*, 5293–5308. [[CrossRef](#)]
17. Ajdari, F.B.; Kowsari, E.; Shahrak, M.N.; Ehsani, A.; Kiaei, Z.; Torkzaban, H.; Ershadi, M.; Eshkalak, S.K.; Haddadi-Asl, V.; Chinnappan, A.; et al. A review on the field patents and recent developments over the application of metal organic frameworks (MOFs) in supercapacitors. *Coord. Chem. Rev.* **2020**, *422*, 213441. [[CrossRef](#)]
18. Jana, S.; Ray, A.; Chandra, A.; Fallah, M.S.E.; Das, S.; Sinha, C. Studies on Magnetic and Dielectric Properties of Antiferromagnetically Coupled Dinuclear Cu(II) in a One-Dimensional Cu(II) Coordination Polymer. *ACS Omega* **2020**, *1*, 274–280. [[CrossRef](#)] [[PubMed](#)]
19. Pettinari, C.; Tombesi, A. MOFs for Electrochemical Energy Conversion and Storage. *Inorganics* **2023**, *11*, 65. [[CrossRef](#)]
20. Li, Y.; Wang, Y.; Fan, W.; Sun, D. Flexible metal-organic frameworks for gas storage and separation. *Dalton Trans.* **2022**, *51*, 4608–4618. [[CrossRef](#)]
21. Xu, B.; Zhang, H.; Mei, H.; Sun, D. Recent progress in metal-organic framework-based supercapacitor electrode materials. *Coord. Chem. Rev.* **2020**, *420*, 213438. [[CrossRef](#)]
22. Rajak, R.; Saraf, M.; Mohammad, A.; Mobin, S.M. Design and construction of a ferrocene based inclined polycatenated Co-MOF for supercapacitor and dye adsorption applications. *J. Mater. Chem. A* **2017**, *5*, 17998–18011. [[CrossRef](#)]
23. Yan, J.; Liu, T.; Liu, X.D.; Yan, Y.H.; Huang, Y. Metal-organic framework-based materials for flexible supercapacitor application. *Coord. Chem. Rev.* **2022**, *452*, 214300. [[CrossRef](#)]
24. Chen, Y.; Kang, C.; Ma, L.; Fu, L.; Li, G.; Hu, Q.; Liu, Q. MOF-derived Fe₂O₃ decorated with MnO₂ nanosheet arrays as anode for high energy density hybrid supercapacitor. *Chem. Eng. J.* **2021**, *417*, 129243. [[CrossRef](#)]
25. Ke, F.-S.; Wu, Y.-S.; Deng, H. Metal-organic frameworks for lithium ion batteries and supercapacitors. *J. Solid. State Chem.* **2015**, *223*, 109–121. [[CrossRef](#)]
26. Xia, W.; Qu, C.; Liang, Z.; Zhao, B.; Dai, S.; Qiu, B.; Jiao, Y.; Zhang, Q.; Huang, X.; Guo, W.; et al. High-Performance Energy Storage and Conversion Materials Derived from a Single Metal-Organic Framework/Graphene Aerogel Composite. *Nano Lett.* **2017**, *17*, 2788–2795. [[CrossRef](#)]
27. Li, M.C.; Wang, W.X.; Yang, M.Y.; Lv, F.C.; Cao, L.J.; Tang, Y.G.; Sun, R.; Lu, Z.G. Large-scale fabrication of porous carbon-decorated iron oxide microcuboids from Fe-MOF as high-performance anode materials for lithium-ion batteries. *RSC Adv.* **2015**, *5*, 7356–7362. [[CrossRef](#)]
28. Xu, Y.; Li, Q.; Guo, X.; Zhang, S.; Li, W.; Pang, H. Metal organic frameworks and their composites for supercapacitor application. *J. Energy Storage* **2022**, *56*, 105819. [[CrossRef](#)]

29. Yang, Q.; Chen, D.; Chu, L.; Wang, J. Enhancement of ionizing radiation-induced catalytic degradation of antibiotics using Fe/C nanomaterials derived from Fe-based MOFs. *J. Hazard. Mater.* **2020**, *389*, 122148. [[CrossRef](#)]
30. Raza, N.; Kumar, T.; Singh, V.; Kiml, K.H. Recent advances in bimetallic metal-organic framework as a potential candidate for supercapacitor electrode material. *Coord. Chem. Rev.* **2021**, *430*, 213660. [[CrossRef](#)]
31. Lee, D.Y.; Yoon, S.J.; Shrestha, N.K.; Lee, S.-H.; Ahn, H.; Han, S.-H. Unusual energy storage and charge retention in Co-based metal-organic-frameworks. *Microporous Mesoporous Mater.* **2012**, *153*, 163–165. [[CrossRef](#)]
32. Yang, J.; Xiong, P.; Zheng, C.; Qiu, H.; Wei, M. Metal-organic frameworks: A new promising class of materials for a high performance supercapacitor electrode. *J. Mater. Chem. A* **2014**, *2*, 16640–16644. [[CrossRef](#)]
33. Lin, X.; Lai, S.; Fang, G.; Li, X. Nickel(II) Cluster-Based Pillar-Layered Metal-Organic Frameworks for High-Performance Supercapacitors. *Inorg. Chem.* **2022**, *61*, 17278–17288. [[CrossRef](#)]
34. Zheng, D.; Wen, H.; Sun, X.; Guan, X.; Zhang, J.; Tian, W.; Feng, H.; Wang, H.; Yao, Y. Ultrathin Mn Doped Ni-MOF Nanosheet Array for Highly Capacitive and Stable Asymmetric Supercapacitor. *Chem. A Eur. J.* **2020**, *26*, 17149–17155. [[CrossRef](#)]
35. Gong, Y.; Li, J.; Jiang, P.G.; Li, Q.F.; Lin, J.H. Novel metal(II) coordination polymers based on N,N'-bis-(4-pyridyl)phthalamide as supercapacitor electrode materials in an aqueous electrolyte. *Dalton T.* **2013**, *5*, 1603–1611. [[CrossRef](#)] [[PubMed](#)]
36. Yang, J.; Zheng, C.; Xiong, P.; Li, Y.; Wei, M. Zn-doped Ni-MOF material with a high supercapacitive performance. *J. Mater. Chem. A* **2014**, *2*, 19005–19010. [[CrossRef](#)]
37. Li, Z.H.; Tan, M.J.; Zheng, Y.H.; Luo, Y.Y.; Jing, Q.S.; Jiang, J.K.; Li, M.J. Application of Conductive Metal Organic Frameworks in Supercapacitors. *J. Inorg. Mater.* **2020**, *7*, 770–780.
38. Hangarter, C.M.; Dyatkin, B.; Laskoski, M.; Palenik, M.C.; Miller, J.B.; Klug, C.A. A Combined Theoretical and Experimental Characterization of a Zirconium MOF with Potential Application to Supercapacitors. *Appl. Magn. Reson.* **2022**, *53*, 915–930. [[CrossRef](#)]
39. Wang, Z.; Gao, C.; Liu, Y.; Li, D.; Chen, W.; Ma, Y.; Wang, C.; Zhang, J. Electrochemical performance and transformation of Co-MOF/reduced graphene oxide composite. *Mater. Lett.* **2017**, *193*, 216–219. [[CrossRef](#)]
40. Campagnol, N.; Romero-Vara, R.; Deleu, W. A hybrid supercapacitor based on porous carbon and the metal-organic framework MIL-100(Fe). *ChemElectroChem* **2014**, *1*, 1182–1188. [[CrossRef](#)]
41. Wang, K.B.; Wang, Z.K.; Wang, X.; Zhou, X.Q.; Tao, Y.H.; Wu, H. Flexible long-chain-linker constructed Ni-based metal-organic frameworks with 1D helical channel and their pseudo-capacitor behavior studies. *J. Power Sources* **2018**, *377*, 44–51. [[CrossRef](#)]
42. Salunkhe, R.R.; Kaneti, Y.V.; Kim, J.; Kim, J.H.; Yamauchi, Y. Nanoarchitectures for metal-organic framework-derived nanoporous carbons toward supercapacitor applications. *Acc. Chem. Res.* **2016**, *12*, 2796–2806.
43. Anaraki, M.A.; Safarifard, A. Fe₃O₄@MOFs magnetic nanocomposites: Synthesis and applications. *Eur. J. Inorg. Chem.* **2020**, *20*, 1916–1937. [[CrossRef](#)]
44. Thakur, B.; Karve, V.V.; Sun, D.T.; Semrau, A.L.; Weiß, L.J.K.; Grob, L.; Fischer, R.A.; Queen, W.L.; Wolfrum, B. An Investigation into the Intrinsic Peroxidase-Like Activity of Fe-MOFs and Fe-MOFs/Polymer Composites. *Adv. Mater. Technol.* **2021**, *6*, 2001048. [[CrossRef](#)]
45. Bi, S.; Banda, H.; Chen, M.; Niu, L.; Wu, T.; Wang, J.; Wang, R.; Feng, J.; Chen, T.; Dincă, M.; et al. Molecular understanding of charge storage and charging dynamics in supercapacitors with MOF electrodes and ionic liquid electrolytes. *Nat. Mater.* **2020**, *19*, 552–558. [[CrossRef](#)] [[PubMed](#)]
46. Yu, Z.y.; Zhang, X.y.; Wei, L.; Guo, X. MOF-derived porous hollow α -Fe₂O₃ microboxes modified by silver nanoclusters for enhanced pseudocapacitive storage. *Appl. Surf. Sci.* **2019**, *463*, 616–625. [[CrossRef](#)]
47. Sui, Y.; Zhang, D.; Han, Y.; Sun, Z.; Qi, J.; Wei, F.; He, Y.; Meng, Q. Effects of Carbonization Temperature on Nature of Nanostructured Electrode Materials Derived from Fe-MOF for Supercapacitors. *Electron. Mater. Lett.* **2018**, *14*, 548–555. [[CrossRef](#)]
48. Bara, D.; Wilson, C.; Mörtel, M.; Khusniyarov, M.M.; Ling, S.L.; Slater, B.; Sproules, S.; Forgan, R.S. Kinetic Control of Interpenetration in Fe-Biphenyl-4,4'-Dicarboxylate Metal-Organic Frameworks by Coordination and Oxidation Modulation. *JACS* **2019**, *20*, 8346–8357.
49. Pan, L.; Nancy, C.; Huang, X.J.; Li, J. Reactions and Reactivity of Co-bpdc Coordination Polymers (bpdc) 4,4'-biphenyldicarboxylate). *Inorg. Chem.* **2000**, *39*, 5333–5340. [[CrossRef](#)]
50. Wang, S.E.; Wang, S.S.; Guo, X.; Wang, Z.K.; Mao, F.F.; Su, L.H.; Wu, H.; Wang, K.B.; Zhang, Q.C. An asymmetric supercapacitor with an interpenetrating crystalline Fe-MOF as the positive electrode and its congenetic derivative as the negative electrode. *Inorg. Chem. Front.* **2021**, *8*, 4878.
51. Jiang, S.; Li, S.; Xu, Y.; Liu, Z.; Weng, S.; Lin, M.; Xu, Y.; Jiao, Y.; Chen, J. An iron based organic framework coated with nickel hydroxide for energy storage, conversion and detection. *J. Colloid. Interface Sci.* **2021**, *600*, 150–160. [[CrossRef](#)]
52. Kaviani, S.; Hajati, S.; Moradi, M. High-rate supercapacitor based on NiCo-MOF-derived porous NiCoP for efficient energy storage. *J. Mater. Sci. Mater. Electron.* **2021**, *32*, 13117–13128. [[CrossRef](#)]
53. Le, K.; Gao, M.J.; Liu, W.; Liu, J.R.; Wang, Z.; Wang, F.L.; Murugadoss, V.; Wu, S.D.; Ding, T.; Guo, Z.H. MOF-derived hierarchical core-shell hollow iron-cobalt sulfides nanoarrays on Ni foam with enhanced electrochemical properties for high energy density asymmetric supercapacitors. *Electrochim. Acta* **2019**, *323*, 134826. [[CrossRef](#)]

54. Lee, C.S.; Moon, J.Y.; Park, J.T.; Kim, J.H. Highly Interconnected Nanorods and Nanosheets Based on a Hierarchically Layered Metal Organic Framework for a flexible, high-performance energy storage device. *ACS Sustain. Chem. Eng.* **2020**, *9*, 3773–3785. [[CrossRef](#)]
55. Pan, Y.; Shi, C.J.; Chen, Y.J.; Li, D.; Tian, Z.; Guo, L.; Wang, Y.Z. Fishbone-like Ni₃S₂/Co₃S₄ integrated with nickel MOF nanosheets for hybrid supercapacitors. *Appl. Surf. Sci.* **2021**, *566*, 150744. [[CrossRef](#)]
56. Zhao, C.; Ding, Y.; Zhu, Z.; Han, S.; Zhao, C.; Chen, G. One-pot construction of highly oriented Co-MOF nanoneedle arrays on Co foam for high-performance supercapacitor. *Nanotechnology* **2021**, *32*, 395606. [[CrossRef](#)]
57. Iqbal, M.Z.; Faisal, M.M.; Ali, S.R.; Fari, R.; Afzal, A.M. Co-MOF/polyaniline-based electrode material for high performance asymmetric supercapacitor devices. *Electrochim. Acta* **2020**, *346*, 136039. [[CrossRef](#)]
58. Alitabar, K.; Zardkhoshoui, A.M.; Davarani, S.S.H. One-step synthesis of porous Ni-Co-Fe-S nanosheet arrays as an efficient battery-type electrode material for hybrid supercapacitors. *Batter. Supercaps* **2020**, *3*, 1311–1320. [[CrossRef](#)]
59. Wang, B.L.; Li, W.; Liu, Z.L.; Duan, Y.J.; Zhao, B.; Wang, Y.; Liu, J.H. Incorporating Ni-MOF structure with polypyrrole: Enhanced capacitive behavior as electrode material for supercapacitor. *RSC Adv.* **2020**, *10*, 12129. [[CrossRef](#)]

Disclaimer/Publisher's Note: The statements, opinions and data contained in all publications are solely those of the individual author(s) and contributor(s) and not of MDPI and/or the editor(s). MDPI and/or the editor(s) disclaim responsibility for any injury to people or property resulting from any ideas, methods, instructions or products referred to in the content.